Theory of transport in silicon quantum wires

G. D. Sanders and C. J. Stanton
Department of Physics, University of Florida, Gainesville, Florida 32611

Y. C. Chang
Department of Physics and Materials Research Laboratory, University of Illinois at Urbana-Champaign, Urbana, Illinois 61801
(Received 16 February 1993; revised manuscript received 17 June 1993)

We calculate transport properties of both electrons and holes in an idealized silicon quantum wire in which scattering is dominated by deformation-potential acoustic-phonon scattering. The quantum-wire electronic states are obtained from an empirical tight-binding calculation while the confined phonon field is treated in a continuum model. Scattering rates within and between quantum-wire subbands are determined from Fermi's golden rule. The method for calculating scattering rates is quite general; we can include any number of electronic and phonon subbands in our theory. To determine transport properties, we use a Monte Carlo approach.

I. INTRODUCTION

The recent observation of efficient luminescence in porous silicon has stimulated a great deal of theoretical and experimental interest in the electronic and optical properties of Si wires.[1-6] The hope is that silicon will finally become a suitable material for optical applications. To achieve this, techniques for fabricating silicon wires reliably and uniformly will be needed. This will stimulate interest not only in the optical properties of porous silicon, but also the transport properties. For instance, to determine the properties of a Si light-emitting diode, one would need to know about the transport properties in addition to the optical properties. In addition, the multivalley nature of the band structure of the quantum wires reported[3] suggests that an intervalley transferred electron effect, leading to a negative differential mobility similar to that seen in GaAs,[7] might be possible in the quantum wires.

In this paper, we study the transport properties of an *ideal* Si quantum-wire structure within the Boltzmann equation framework. While such ideal wires do not currently exist, it is hoped that by studying ideal wires, insight will be gained into more general wire structures. To determine the energy bands, we utilize the empirical tight-binding method described in Ref. 3. In comparison with GaAs wires,[8] transport in silicon wires is easier to model since silicon is a nonpolar material and the dominant scattering mechanism (in the absence of impurities) is deformation-potential phonon scattering. While in actual bulk silicon, the phonon scattering can be quite complicated involving both acoustic intravalley and acoustic and optical intervalley scattering (of both f and g type),[9] in our ideal model we consider scattering only with a "generic" acoustic phonon. We develop a procedure for calculating the acoustic deformation-potential scattering rates both *within* and *between* quantum-wire subband states, within the framework of Fermi's golden rule. In calculating the scattering rates, we incorporate tight-binding subbands and wave functions determined from the tight-binding band-structure calculation. Unlike GaAs wires, where the wires are not free standing, the phonon modes in the Si wires are quantized. We allow for *quantum confined phonons* within a continuum model. This method of calculating scattering rates treats all initial and final subband states on an equal footing and automatically takes subband mixing, level crossings, and Bloch form factors into account.

Once the scattering rates are obtained, the transport properties can be determined by solving the Boltzmann transport equation. To solve the Boltzmann equation, we adopt the Monte Carlo method.[10,11] The Monte Carlo method has the advantage of being able to handle many different scattering mechanisms as well as incorporating realistic band structures.[12]

In Sec. II we discuss the theory used in calculating the transport properties of the silicon wires and in Sec. III we present our results.

II. THEORY

To determine the transport properties of silicon quantum wires, several steps need to be taken. First, the wire geometry and band structure must be determined so that the electronic states are known. For the states in GaAs, oftentimes a simple envelope approximation works for determining the states and wave functions. This is not the case in Si since the lowest-lying conduction state is in the X valley and is not direct. After the electronic states are known, the scattering rates need to be determined. Finally, the scattering rates and electronic states are then used as input into the Boltzmann transport equation, and the transport properties of the system are determined.

A. Wire geometry and band structure

In our *ideal* wire geometry, we consider an infinitely long silicon wire oriented along (001) with a square cross section whose faces, of length L, are parallel to the four equivalent (110) planes. In addition, all the silicon dangling bonds at the surface are assumed to be passivated

by hydrogen derived from the HF acid used in fabrication. The quantum-wire crystal structure is shown in Fig. 1. The basic unit (shown in the upper portion of Fig. 1), from which we construct the quantum wire, contains four silicon atoms and has a height a and width $a/\sqrt{2}$, where a is the lattice constant ($a=5.43$ Å for Si). The quantum-wire unit cell (a cross-sectional slab) consists of $N\times N$ such basic unit cells and there are an infinite number of these slabs stacked on top of each other along the [001] wire axis. The width of the wire is $L=Na/\sqrt{2}$. The quantum-wire Brillouin zone is one dimensional since the crystal structure is only periodic along the [100] wire axis. Note that the Brillouin-zone boundary in the [100] direction for the quantum wire occurs at π/a as opposed to $2\pi/a$ for bulk silicon. This is associated with a doubling of the repeat distance in the wire, illustrated in Fig. 1.

To obtain the electronic properties of free-standing silicon quantum wires, we use a second-neighbor empirical tight-binding model which includes seven atomic orbitals per silicon site with symmetries s,x,y,z,d_1,d_2, and s^*, where $d_1=(x^2-y^2)/\sqrt{2}$ and $d_2=(3z^2-r^2)/\sqrt{6}$. Bulk silicon has T_d point-group symmetry and the d-like orbitals decompose into two d^2 orbitals which transform according to the E representation, plus three d^3 orbitals which transform according to the T_2 representation.

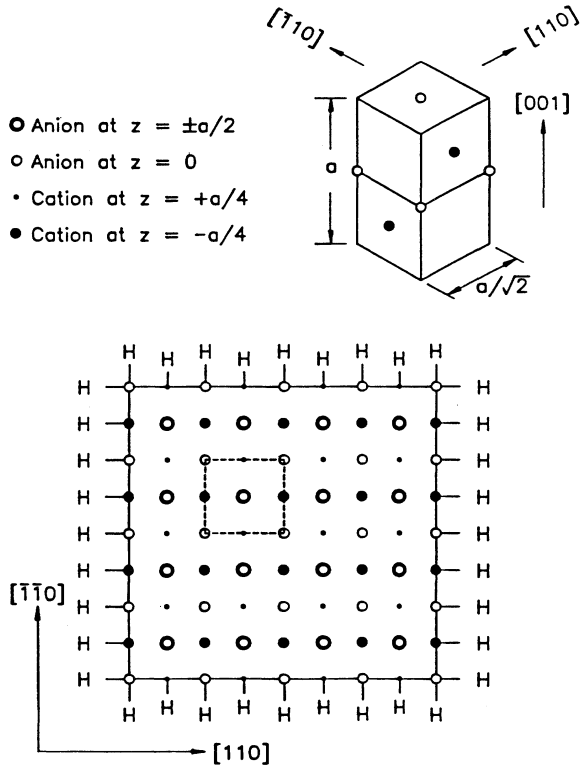

FIG. 1. Crystal structure of an idealized silicon quantum wire. The base unit, shown in the upper portion of the figure, contains four silicon atoms. The quantum-wire unit cell is a cross-sectional slab consisting of $N\times N$ such basic units. The faces, of width L, are parallel to the four equivalent (110) planes and the wire axis is oriented along [001].

Since the d^3 orbitals have the same symmetry as the p orbitals, their role is already taken up by the p orbitals, and they can be excluded for simplicity. The s^* orbital, as originally introduced by Vogel, Hjalmarson, and Dow,[13] is added to improve the description of higher conduction bands.

We retain second-neighbor interactions, because in a nearest-neighbor model, the transverse effective mass at the X point is *infinite*. Since the quantum-confinement energies for X-like conduction-band states are governed by the X-valley transverse mass, it is essential to include the second-neighbor interactions.

Hamiltonian matrix elements between silicon atomic orbitals are obtained by fitting tight-binding bands for bulk silicon to corresponding results from an empirical pseudopotential calculation in bulk silicon.[14] In the energy range of interest, our model closely matches the pseudopotential results throughout the entire Brillouin zone.[3]

We neglect reconstruction of the hydrogen passivated surfaces. The surface hydrogen contains a single s orbital and all Hamiltonian and optical matrix elements between silicon orbitals and hydrogen s states are scaled according to the $1/d^2$ rule.[15] Since the radius of hydrogen is much less than the silicon radius, we take d to be half the Si-Si bond length.

Using the tight-binding Hamiltonian matrix elements between localized atomic orbitals, we compute the subband structure $E_n(k)$ and the tight-binding wave functions for the idealized quantum wire using the slab method. The tight-binding wave functions are expressed as Bloch sums

$$\varphi_{nk}(\mathbf{r})=\sum_{\mathbf{R}_0,L,\alpha} Z^n_{\mathbf{R}_0,\alpha}(k)\frac{e^{ikLa}}{\sqrt{N}}\phi_\alpha(\mathbf{r}-\mathbf{R}_0-La\hat{\mathbf{z}}) , \quad (1)$$

where N is the number of slabs, $\mathbf{R}_0$ denotes atomic sites within a cross-sectional slab, L labels the slab, and α labels the orbital. The tight-binding expansion coefficients are $Z^n_{\mathbf{R}_0,\alpha}(k)$ and $\phi_\alpha(\mathbf{r}-\mathbf{R}_0-La\hat{\mathbf{z}})$ is localized atomic orbital of symmetry type α centered at position R_0 within slab L. A reduction in the size of the tight-binding Hamiltonian matrix is obtained by exploiting mirror symmetry about the perpendicular mirror planes (110) and ($\bar{1}$10). We consider symmetrized tight-binding wave functions labeled by (+,+), (−,+), (+,−), and (−,−) where the two indices label the parity about (110) and ($\bar{1}$10), respectively. In this basis, the Hamiltonian is block diagonal with four blocks corresponding to the four symmetry types.

B. Scattering rates and phonon states

Since silicon is nonpolar, the dominant scattering mechanism at room temperature and low fields is deformation-potential phonon scattering. In bulk silicon, phonon scattering can either be intervalley or intravalley. Intravalley scattering is usually acoustic. Intervalley scattering can be either acoustic or optic depending on whether the scattering is f or g type, and depending on the value for the deformation potential constant. Intervalley scattering in bulk Si can occur via acoustic-phonon

scattering; however, due to the large change in wave vector, this type of scattering involves a finite energy for the acoustic phonon, the lowest energy being about 10 meV.[9] In this paper, in keeping with the simplicity of the model, we consider scattering only by acoustic phonons. However, for electric fields which are sufficiently high to create a significant number of carriers above the optic-phonon frequency (63 meV) deformation-potential scattering by optical phonons can also be important and must be included. Impurity scattering for heavily doped material can also be important and limit the mobility, but we will assume that the samples are clean enough so that the mobility is not dominated by impurity scattering. Finally, at high carrier densities, carrier-carrier scattering can become important. For intraband scattering in one-dimension, this is not very important since carrier-carrier scattering is a small q interaction which favors forward scattering. It can, however, become important for interband scattering. We will assume that the densities are low enough so that carrier-carrier scattering is not an important effect. Thus our calculation is applicable to carrier densities below $\approx 10^{16}/\text{cm}^3$ and at room temperature. Above these densities, carrier-carrier as well as impurity scattering can become more important. As can be seen, not only is the geometry and electronic structure of the wire treated in an ideal model, but also the scattering. In "real" wires, surface roughness and deviations from the ideal cross section must also be taken into account. These will further limit the mobility of such wires. Our calculation thus represents a "best case" scenario.

The electron-phonon interaction energy is given by

$$H_{ep}=\epsilon_1 \nabla\cdot\mathbf{u}(\mathbf{r}) \tag{2}$$

where ϵ_1 is the isotropic deformation potential for bulk silicon and u_j is the jth component of the ion displacement. For electrons, $\epsilon_1=9.5$ eV and for holes $\epsilon_1=5.0$ eV.[16]

In GaAs wires, the wire is created by confining electrons in a quasi-one-dimensional potential due to the AlGaAs/GaAs interface and the phonons can be treated as bulklike. In the free-standing silicon wires considered here, the phonons are quantum confined. For quantum-confined phonons in free-standing silicon wires, we adopt a continuum model in which the phonon Hamiltonian in a silicon wire of size L is given by

$$H_p=\sum_{ll'q}\hbar\omega_{ll'q}a^{\dagger}_{ll'q}a_{ll'q} \ . \tag{3}$$

The phonons are assumed to be in thermal equilibrium (we neglect hot-phonon effects) and the dispersion relation is

$$\omega_{ll'q}=c_s\sqrt{q^2+q_l^2+q_{l'}^2} \ , \tag{4}$$

where $q_l=l\pi/L$ and $q_{l'}=l'\pi/L$ are the lth and l'th quantized phonon wave vectors along the [100] and [010] confinement directions, $c_s=9.04\times10^5$ cm/sec is the longitudinal sound speed in bulk silicon, and q is the phonon wave vector along the [001] wire axis. Following standard convention, $a^{\dagger}_{ll'q}$ and $a_{ll'q}$ are phonon creation and destruction operators. Since the $l=l'=0$ phonon branch is of the form $\omega=c_sq$, we refer to phonons in this branch as acoustic phonons. Phonons in higher-lying phonon branches are referred to as excited quantum-confined phonons. This is illustrated in Fig. 2 where we plot the phonon energies as a function of wave vector for the lowest phonon modes in a 7.7-Å wire.

The number of longitudinal acoustic phonon modes N_p is equal to the number of silicon atoms in the wire. Thus

$$N_p=\frac{AL_z}{v_c} \ , \tag{5}$$

where A is the cross-sectional area of the wire, L_z is the length of the wire along the growth direction, and $v_c=a_0^3/8$ is the volume of the Wigner-Seitz cell associated with a silicon atom. In a continuum model, the number of phonon modes is infinite. To correct for this, we introduce a *Debye cutoff* for the quantum-confined phonon-dispersion relation. The Debye cutoff energy $\hbar\omega_D$ is defined by requiring that the total number of phonon modes (obtained by integrating over the phonon density of states) be given by N_p. Thus

$$N_p=\int_0^{\hbar\omega_D}\rho(E)dE=\int_0^{\hbar\omega_D}\sum_{ll'q}\delta[E-\hbar\omega_{ll'(q)}]dE \tag{6}$$

defines the Debye cutoff energy.

The ion displacements for the continuum phonon field can be expressed in terms of plane waves

$$\mathbf{u}(\mathbf{r})=\sum_{ll'q}\left[\frac{\hbar}{2\rho V\omega_{ll'q}}\right]^{1/2}\frac{\mathbf{Q}_{ll'q}}{\sqrt{q^2+q_l^2+q_{l'}^2}}\times(a_{ll'q}+a^{\dagger}_{ll'q})e^{i\mathbf{Q}_{ll'}\cdot\mathbf{r}} \ . \tag{7}$$

where $\mathbf{Q}_{ll'q}=(q_l,q_{l'}q)$ is the total phonon wave vector. Substitution of the phonon displacement field into the deformation-potential electron-phonon Hamiltonian yields

$$H_{ep}(\mathbf{r})=i\epsilon_1\sum_{ll'q}\left[\frac{\hbar}{2\rho V\omega_{ll'q}}\right]^{1/2}\sqrt{q_l^2+q_{l'}^2+q^2}\times(a_{ll'q}+a^{\dagger}_{ll'q})e^{i\mathbf{Q}_{ll'q}\cdot\mathbf{r}} \ . \tag{8}$$

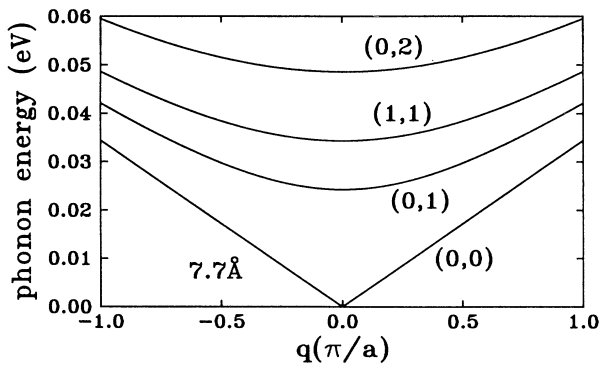

FIG. 2. Quantum confined phonon-dispersion relations for a 7.7-Å quantum wire. The phonon modes are labeled by the phonon quantum numbers (l,l').

In second quantized form the electron-phonon interaction is given by

$$\hat{\mathbf{H}}_{ep}=\int \psi^{\dagger}(\mathbf{r})H_{ep}(\mathbf{r})\psi(\mathbf{r})d\mathbf{r} , \tag{9}$$

where $\psi^{\dagger}(\mathbf{r})$ is the field operator associated with the creation of an electron at position $\mathbf{r}$ and is related to the tight-binding wave functions $\varphi_{n,k}(\mathbf{r})$ by

$$\psi^{\dagger}(\mathbf{r})=\sum_{nk}\varphi^{*}_{nk}(\mathbf{r})c^{\dagger}_{nk} . \tag{10}$$

Here the operator $c^{\dagger}_{nk}$ creates an electron in a quantum-wire state with subband index n and wave vector k.

Performing the indicated integration over position, the electron-phonon interaction becomes

$$\hat{\mathbf{H}}_{ep}=i\epsilon_1\sum_{ll'q}\left[\frac{\hbar}{2\rho V\omega_{ll'q}}\right]^{1/2}\sqrt{q_l^2+q_{l'}^2+q^2}\times(a_{ll'q}+a^{\dagger}_{-ll'q})G_{ll'}(q) , \tag{11}$$

where

$$G_{ll'}(q)=\int \psi^{\dagger}(\mathbf{r})e^{i\mathbf{Q}_{ll'q}\cdot\mathbf{r}}\psi(\mathbf{r})d\mathbf{r} \tag{12}$$

is an overlap form factor which is written in terms of the atomic orbitals as

$$G_{ll'}=\sum_{nk}\sum_{n'k'}c^{\dagger}_{nk}c_{n'k'}\sum_{\mathbf{R}_0,L,\alpha}Z^{n*}_{\mathbf{R}_0,\alpha}(k)\frac{e^{-ikLa}}{\sqrt{N}}\sum_{\mathbf{R}'_0,L',\alpha'}Z^{n'}_{\mathbf{R}'_0,\alpha'}(k')\frac{e^{ik'L'a}}{\sqrt{N}}\int\phi^{*}_{\alpha}(\mathbf{r}-\mathbf{R}_0-La\hat{\mathbf{z}})e^{i\mathbf{Q}_{ll'q}\cdot\mathbf{r}}\phi_{\alpha'}(\mathbf{r}-\mathbf{R}'_0-L'a\hat{\mathbf{z}})d\mathbf{r} . \tag{13}$$

In evaluating the integrals over localized atomic orbitals, we neglect two-center integrals in comparison with on-site integrals. For small $\mathbf{Q}_{ll'q}$ scattering, the exponential factor is slowly varying over atomic dimensions and can be treated as a constant to be taken outside the integral. Thus

$$\int\phi^{*}_{\alpha}(\mathbf{r}-\mathbf{R}_0-La\hat{\mathbf{z}})e^{i\mathbf{Q}_{ll'q}\cdot\mathbf{r}}\phi_{\alpha'}(\mathbf{r}-\mathbf{R}'_0-L'a\hat{\mathbf{z}})d\mathbf{r}=e^{i\mathbf{Q}_{ll'q}\cdot\mathbf{R}_0}(e^{iqLa}\delta_{\alpha\alpha'}\delta_{\mathbf{R}_0\mathbf{R}'_0}\delta_{LL'}) \tag{14}$$

and the form factor simplifies to

$$G_{ll}(q)=\sum_{nk}\sum_{n'k'}c^{\dagger}_{nk}c_{n'k'}\left[\sum_{\mathbf{R}_0\alpha}Z^{n*}_{\mathbf{R}_0,\alpha}(k)Z^{n'}_{\mathbf{R}_0,\alpha}(k)e^{i\mathbf{Q}ll'q\cdot\mathbf{R}_0}\right]\times\left[\frac{1}{N}\sum_{L}e^{i(k'+q-k)La}\right] . \tag{15}$$

The sum over L gives the selection rule

$$\frac{1}{N}\sum_{L}e^{i(k'+q-k)La}=\delta_{k'-k-\Gamma_m,q} \tag{16}$$

where $\Gamma_m=2\pi m/a$ is a reciprocal-lattice vector in the quantum-wire Brillouin zone and δ is the Kronecker delta function. If we ignore umklapp processes and thus set $\Gamma_m=0$, we obtain

$$G_{ll'}(q)=\sum_{nk}\sum_{n'k'}c^{\dagger}_{nk}c_{n'k'}\left[\sum_{\mathbf{R}_0,\alpha}Z^{n*}_{\mathbf{R}_0,\alpha}(k)Z^{n'}_{\mathbf{R}_0,\alpha}(k')e^{i\mathbf{Q}_{ll'q}\cdot\mathbf{R}_0}\right]\times\delta_{k'-k,q} , \tag{17}$$

where the sum over site coordinates is restricted to a quantum-wire unit cell of height a and cross-sectional area A.

The scattering rates are obtained from Fermi's golden rule. The electron-scattering rate from state n,k to state n',k' due to emission and absorption of quantum-confined phonons with quantum numbers l and l' is

$$W^{nn'}_{kk'}(ll')=\frac{\pi\epsilon_1^2}{\rho V\omega_{ll'q}}|G^{nn'}_{kk'}(ll')|^2[q_l^2+q_{l'}^2+(k-k')^2]\times\{N_{ll'q}\delta[E_{n'}(k')-E_n(k)-\hbar\omega_{ll'q}]+(N_{ll'q}+1)\delta[E_{n'}(k')-E_n(k)+\hbar\omega_{ll'q}]\} , \tag{18}$$

where $N_{ll'q}$ is the equilibrium occupation number for phonons with energy $\hbar\omega_{ll'q}$. The form factor is

$$|G^{nn'}_{kk'}(ll')|^2=\left|\sum_{\mathbf{R}_0,\alpha}Z^{n}_{\mathbf{R}_0,\alpha}(k)^{*}Z^{n'}_{\mathbf{R}_0,\alpha}(k')\times e^{i(q_lR_{0x}+q_{l'}R_{0y}+(k-k')R_{0z})}\right|^2 , \tag{19}$$

which can be evaluated in terms of the quantum-wire tight-binding expansion coefficients. Note that for the ground-state phonon ($l=l'=0$), the form factor approaches unity for $k\approx k'$ since the form factor reduces to the wave-function overlap for $\varphi_{nk}(\mathbf{r})$.

The total scattering rate due to emission and adsorption of quantum-confined phonons is obtained by summing over all phonon quantum numbers l and l'. Thus

$$W^{nn'}_{kk'}=\sum_{ll'}W^{nn'}_{kk'}(ll') . \tag{20}$$

C. Solution of the Boltzmann transport equation

To solve the Boltzmann transport equation by the Monte Carlo method, we define a steady-state distribution function $f_n(k)$ for each quantum-wire subband n. We divide k space into evenly spaced k cells of width $\Delta k=2\pi/aN_k$ where N_k is the number of cells and the k value at the midpoint of each cell is k_m ($m=1,\ldots,N_k$). We wish to evaluate the average distribution function $f_n(k_m)$ in each of these cells.

The rate at which electrons in subband n with wave vector k are scattered into other states is given by

$$\Gamma_k^n = \sum_{n'k'} W_{kk'}^{nn'} \ . \tag{21}$$

The scattering-out rate for an electron in cell m is obtained by averaging over initial states. Thus

$$\Gamma_m^n = \frac{1}{\Delta k} \int_{k_m-\Delta k/2}^{k_m+\Delta k/2} dk \ \Gamma_k^n \ . \tag{22}$$

Converting the sum over k' to an integral, we obtain

$$\Gamma_m^n = \sum_{n'm'} W_{mm'}^{nn'} \ , \tag{23}$$

where

$$W_{mm'}^{nn'} = \frac{1}{\Delta k} \frac{L_z}{2\pi} \int_{k_m-\Delta k/2}^{k_m+\Delta k/2} \int_{k_{m'}-\Delta k/2}^{k_{m'}+\Delta k/2} W_{kk'}^{nn'} dk \ dk' \tag{24}$$

is an average of the microscopic scattering rates over initial and final k cells m and m'. For each subband n and wave vector k_m, we evaluate tight-binding energy bands and wave functions. The scattering rates $W_{mm'}^{nn'}$ are then determined by numerical integration and tabulated. In performing the double integrals, the energy-conserving δ functions in the microscopic scattering rates are replaced by Lorentzians of half width $\gamma = 2\times10^{-5}$ eV and the subband energies and form factors are evaluated by linear interpolation.

After the scattering rates are tabulated, we use Monte Carlo simulation of a carrier trajectory to obtain the distribution functions $f_n(k_m)$. Free-flight times are selected by introducing the usual self-scattering mechanism to obtain a constant total scattering rate for carriers initially in subband n. The wave vector k_f at the end of the free flight is given in terms of the initial wave vector k_i and the free-flight time $t_f - t_i$ by the semiclassical expression $k_f = k_i - (eF/\hbar)(t_f - t_i)$ with F being the electric field. The wave vector k_i is used to assign the carrier to an initial k cell m. The scattering event terminating the free flight is determined randomly based on the rates for transitions out of the initial state. If the carrier scatters to subband n' and k cell m' the carrier subband index is updated to n' and the wave vector is updated by adding $\Delta k = k_{m'} - k_m$ to k_i. If a self-scattering is selected, we set $n' = n$ and $m' = m$ and proceed to the next scattering event. After each non-self-scattering event, we note which subband and k cell the carrier is in and use this information to create a histogram of $f_n(k_m)$.

Once the distribution functions are determined, the carrier drift velocity v_d can be readily obtained as

$$v_d = \frac{\sum_{nm} \int_{k_m-\Delta k/2}^{k_m+\Delta k/2} f_n(k) v_n(k)}{\sum_{nm} \int_{k_m-\Delta k/2}^{k_m+\Delta k/2} f_n(k)} \tag{25}$$

where

$$v_n(k) = \frac{1}{\hbar} \frac{dE_n(k)}{dk} \tag{26}$$

is the group velocity of an electron in quantum wire in subband n with wave vector k. Approximating the derivative of the band structure by a two-point difference formula, we obtain

$$v_d = \frac{1}{\hbar} \frac{\sum_{nm,} f_n(k_m)[E_n(k_m+\Delta k/2) - E_n(k_m-\Delta k/2)]}{\sum_{nm} f_n(k_m)\Delta k} \tag{27}$$

for the carrier velocity. Velocity-field curves are obtained by plotting drift velocity as a function of applied field and low-field mobilities are obtained from the slope of the velocity-field curves at $F = 0$.

III. RESULTS AND DISCUSSION

A. Band structure

We have calculated quantum-wire band structures for several wire widths. The computed band structures are shown in Fig. 3 for quantum wires with $L = 7.7$, 15.4, and 23 Å. The Brillouin zone is one dimensional since the wire is only periodic along [001]. The repeat distance along this direction is $a = 5.43$ Å whereas in bulk Si is the repeat distance is $a/2$. Thus the quantum-wire Brillouin zone is half the bulk Brillouin zone along [001]. Although bulk Si is indirect, the Si wire band structure is seen to be pseudodirect with an X-like conduction-band minimum and a Γ-like valence-band maximum at the zone center.

The direct conduction band in a quantum wire can be qualitatively explained. In bulk Si, the indirect conduction band consists of six equivalent X valleys with minima at $\pm 0.85(2\pi/a)$ along $\langle 100 \rangle$ directions. These valleys are anisotropic ellipsoids with two transverse masses of $0.19m_0$ and a heavy longitudinal mass of $0.92m_0$. In quantum wires, the projections of four of these valley minima (oriented along the [100] and [010] directions) onto the wire axis are at the zone center and their energies determined by the effective masses along the [110] and [$\bar{1}$10] confinement direction. When projected onto the [001] wire axis, these states give rise to the four closely spaced, direct conduction subbands seen in Fig. 3.

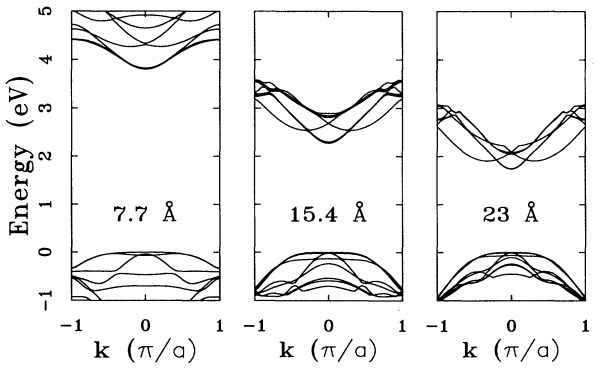

FIG. 3. Band structures of Si quantum wires (a) $L = 7.7$ Å, (b) $L = 15.4$ Å, and (c) $L = 23$ Å. The Brillouin zone is one dimensional with k ranging from $-\pi/a$ to $+\pi/a$.

Each subband consists of substantial admixtures of bulk states derived from the four degenerate X valleys and we have a strong intervalley mixing effect.

The quantum-wire subbands derived from the two X valley along [001] are indirect since the projections of their valley minima onto the wire axis are near $\pm 0.85(2\pi/a)$, which becomes $\pm 0.3(\pi/a)$ after mapping into the quantum-wire Brillouin zone (since the Brillouin-zone periodicity is the twice the bulk as explained earlier). The states derived from the two X valleys along [001] have higher energies than the direct minima since the [001] valleys have light transverse masses along both confinement directions. The indirect minimum at $k \approx 0.3\pi/a$ are clearly seen in Fig. 3, although in Fig. 3(a), the band hybridization makes them difficult to see.

The valence bands are Γ-like. At $k=0$, the highest-lying state (or the top valence band) has $(+,+)$ symmetry and consists of predominantly z-like atomic orbitals. It is, of course, direct in both bulk silicon and in the wire. As the silicon wire is made smaller, the size of the direct gap increases as can be seen in Fig. 3. The electronic structure of the silicon wire with a direct, low mass valley and high mass satellite valleys suggests a transferred valley effect leading to negative differential mobilities and a Gunn effect similar to that in bulk GaAs might be observed in silicon quantum wires. This partially motivates a study of the transport properties of the wire.

B. Scattering rates

The transition rate for scattering out of the k cell m in subband n to any k cell in subband n' is given by $\Gamma_m^{nn'} = \sum_{m'} W_{mm'}^{nn'}$. The total scattering-out rate, obtained by summing over all final subband states, is $\Gamma_m^n = \sum_{n'} \Gamma_m^{nn'} = \sum_{n'm'} W_{mm'}^{nn'}$.

We plot scattering-out rates for electrons and holes in a 7.7-Å quantum wire at $T=300$ K. In Fig. 4 we plot $\Gamma_m^{nn'}$ and Γ_m^n as functions of k_m for scattering from an initial subband n to all final subbands n'. The conduction subbands are shown in Fig. 4(a).

In Fig. 4(b) we plot scattering-out rates for initial states in the first quantum-wire conduction subband. The sharp peak in the scattering rate at $k_m=0$ is due to emission and absorption of acoustic phonons ($l=l'=0$ and $\omega=c_s q$). The acoustic-phonon population is approximately given by the equipartition expression $N_q \approx (k_B T/\hbar\omega) - \frac{1}{2}$ and the form factor simplifies to $|G_{kk'}^{nn'}(0,0,)|^2 \approx \delta_{nn'}$. If we neglect phonon energies in comparison with electron energies and assume a parabolic band with effective mass m_e, we see that the scattering-out rate due to emission and absorption of acoustic phonons is approximately

$$\Gamma_1(k) \approx \frac{\epsilon_1^2 k_B T}{\rho A \hbar c_s^2} \int \delta[E_1(k') - E_1(k)]dk' \approx \frac{\epsilon_1^2 k_B T}{\rho A \hbar c_s^2} \frac{2m_e}{\hbar^2 |k|} . \quad (28)$$

The sharp peak in the cell-averaged scattering rate near the zone center is due to the enhanced density of states at the conduction-band edge and falls off roughly as k_m^{-1}. Clearly the broadening factor γ keeps the rate from being infinite. Electrons initially in the first conduction subband are primarily scattered back to the first subband, but we note that some scattering to the second subband near the zone center is allowed as can be seen in Fig. 4(b).

In Fig. 4(b) a sharp increase in the scattering-out rate is seen near $k=0.1\pi/a$. This enhanced scattering is due to spontaneous emission of quantum-confined phonons. The confined phonon bands are not thermally populated

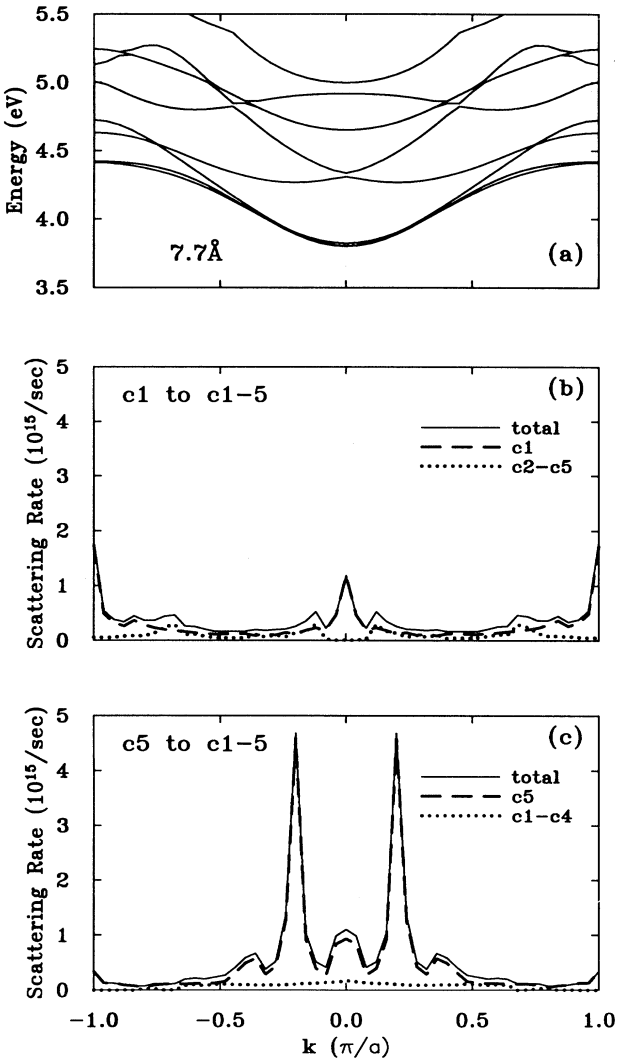

FIG. 4. Acoustic deformation-potential scattering-out rates for electrons in a 7.7-Å silicon quantum wire at 300 K. The conduction-band structure is shown in (a), scattering-out rates for electrons in the first conduction subbands are shown in (b), while scattering-out rates for electrons in the fifth conduction subband are shown in (c). The scattering-out rates are k dependent and are symmetric about $k=0$. The solid line is the total scattering-out rate for an electron with wave vector k while the other lines represent the scattering out rates into a specific subband.

due to their higher energy, so we can set $N_{ll'g} \approx 0$ in the expression for the scattering rate. If we take the phonon dispersion to be constant over wave vectors of interest, neglect the form factors between different subbands, and assume parabolic bands, the scattering-out rate due to spontaneous emission of quantum-confined phonons is approximately

$$\Gamma_2(k) \approx \frac{\epsilon_1^2}{2\rho A \hbar c_s^2} \sum_{ll'} |G(ll')|^2 \hbar\omega_{ll',0} \int \delta[E_1(k') - E_1(k) - \hbar\omega_{ll',0}] dk'$$
$$\approx \frac{\epsilon_1^2}{2\rho A \hbar c_s^2} \sum_{ll'} |G(ll')|^2 \hbar\omega_{ll',0} \frac{2m_e}{\hbar^2 |k| \sqrt{1 - \hbar\omega_{ll',0}/E_1(k)}} . \quad (29)$$

In the above expression, scattering by spontaneous emission of confined phonons is only defined at values of k where the electron energy exceeds the quantum-confined phonon energy. As electrons are accelerated to higher energies, the number of quantum-confined phonon bands available for scattering increases. The form factors can be estimated in an effective-mass picture by replacing the tight-binding wave functions with a continuous ground-state envelope function. Thus

$$G(ll') \approx \frac{4}{L^2} \int_{-L/2}^{L/2} \cos^2(\pi x/L) e^{iq_l x} dx \times \int_{-L/2}^{L/2} \cos^2(\pi y/L) e^{iq_{l'} y} dy . \quad (30)$$

This integral is unity for the lowest phonon branch ($l = l' = 0$) and decreases rapidly with l and l' due to the rapidly oscillating exponentials in the integrand.

Scattering between different subbands is possible because of nonzero form factors between initial and final states. In Fig. 4(b) we see that electrons in the first conduction subband may scatter into higher subbands. For values of k near the zone boundary, the scattering rate is enhanced due to the large density of states.

The scattering-out rates for the first four nearly degenerate lowest-lying conduction subbands are very similar. In Fig. 4(c) we show the scattering-out rates for electrons in the fifth conduction subband. This band includes the two satellite valleys near $\pm 0.3\pi/a$ as can be seen in Fig. 4(a). In this case we see two sharp peaks in the scattering-out rates centered at the minima of the two satellite valleys. As in the case of the single valley centered at $k = 0$, these two peaks are due to emission and absorption of acoustic phonons (the ground-state phonon band) near the bottom of the satellite valleys, while the nearby side peaks are again due to spontaneous emission of higher-lying quantum-confined phonons. As can be seen from Figs. 4(b) and 4(c), the scattering rates become large in small wires. For scattering rates this large, corrections to the golden rule should be included to more accurately determine the rates.

C. Distribution functions

We have studied room-temperature electron-distribution functions $f_n(k)$ in 7.7- and 15.4-Å quantum wires. In Fig. 5 we show room-temperature electron-distribution functions for a 7.7-Å quantum wire in the ab-

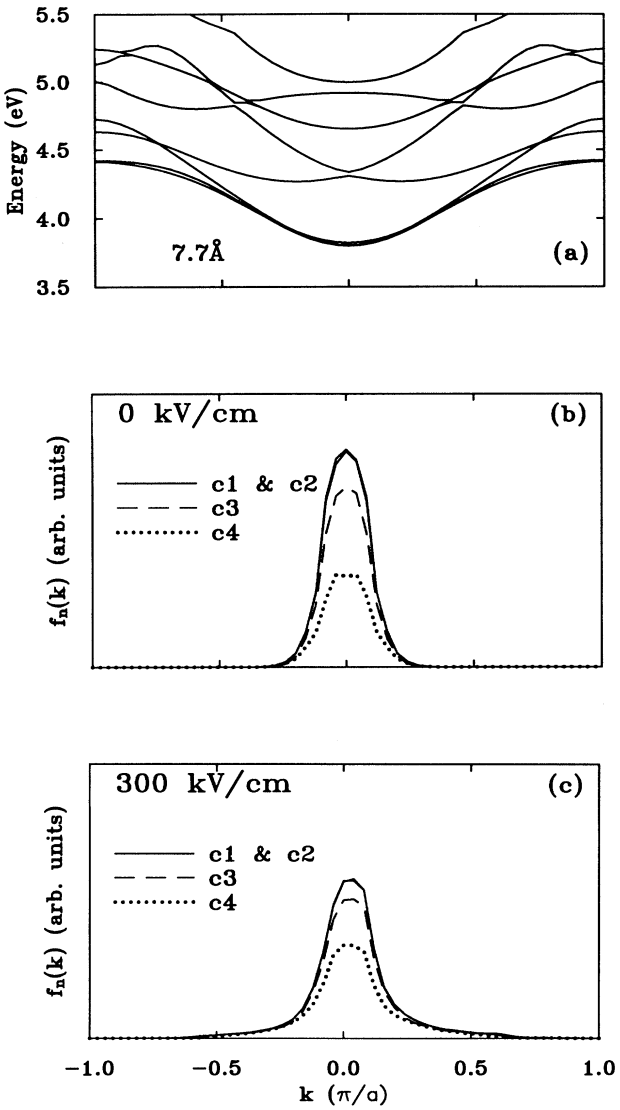

FIG. 5. Electron distribution functions in a 7.7-Å silicon quantum wire at 300 K. The conduction-band structure is shown in (a) for comparison. The electron distribution functions are shown in (b) in the absence of an electric field and in (c) with an applied field of 300 kV/cm. For this case, the band-edge mobilities are very low and the electrons are confined to the bottom four condition subbands.

sence of an electric field [Fig. 5(b)] and with a field of 300 kV/cm [Fig. 5(c)]. In our convention, the electric field points to the left and electrons drift to the right. In the absence of an electric field, we recover the equilibrium distributions which are given explicitly by $f_n(k) \propto e^{-[E_n(k)/kT]}$. In n-type wires the four pseudodirect conduction-subband minima at the zone center are heavily populated while the higher-lying subbands are empty. In the presence of an electric field, the electron distributions are distorted and displaced to the right, giving rise to a net positive drift velocity for electrons and negative current density. In the 7.7-Å wire, the scattering rates are very high and band-edge mobilities are very low. Consequently, the electrons are confined to the vicinity of the band edge even at very high fields.

In Fig. 6 we plot room-temperature distribution functions for a 15.4-Å quantum wire. The quantum-wire bands are shown in Fig. 6(a) and the distribution functions are shown in Fig. 6(b) and 6(c) in the absence of an electric field and with an electric field of 105 kV/cm. As can be seen in the figure, only the lowest four bands are populated at room temperature in the absence of an electric field. With an applied field of 105 kV/cm, we see a significant scattering into higher-lying subbands. In particular, we note that the two satellite valleys are populated.

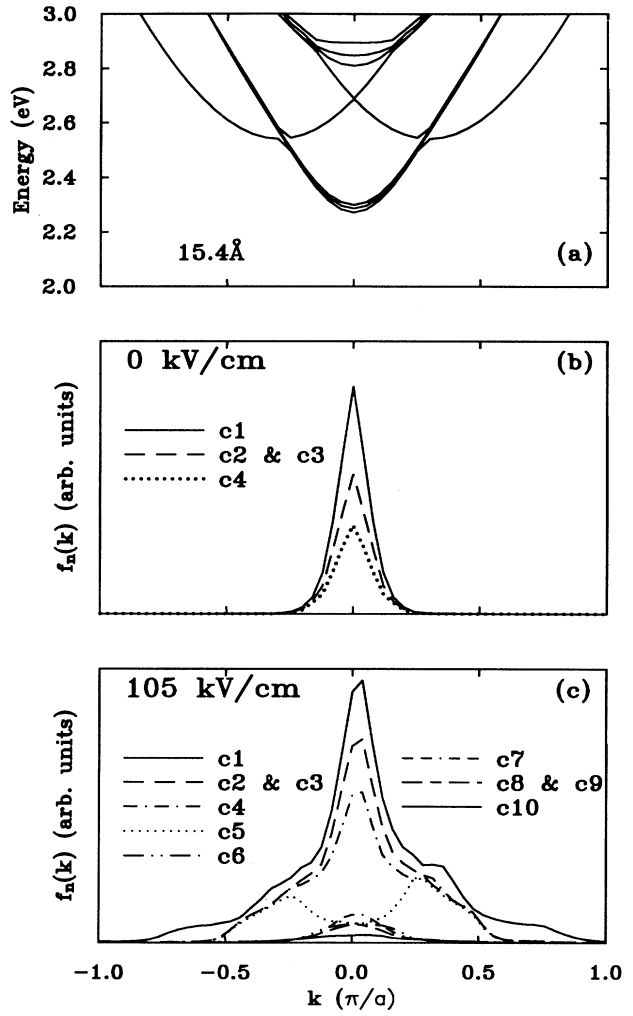

FIG. 6. Electron distribution functions in a 15.4-Å silicon quantum wire at 300 K. The conduction-band structure is shown in (a), the distribution functions in the absence of an electric field are shown in (b), and the distribution functions in the presence of a 105-kV/cm electric field are shown in (c). In the absence of an electric field, only the bottom four conduction subbands are populated at room temperature. When an electric field is applied, carriers are scattered into higher subbands.

D. Low-field mobilities

Low-field electron and hole mobilities at 300 K are shown in Fig. 7 for wire widths between 7.7 and 23 Å. The electron mobilities depend on wire size and vanish as $L \rightarrow 0$. For electrons, low-field mobilities can be estimated in a simplified relaxation-time approximation. In thermal equilibrium, we have seen that the electron-distribution functions are localized near the bottom of the four pseudodirect valleys. These bands all have approximately the same effective mass and there is little scattering among them at small values of k. Thus, electrons in the four valleys behave almost identically and we need only consider an electron in a single parabolic band. The electron mobility is given by $\mu = e\tau/m$, where m is the electron effective mass and τ is the relaxation time. The relaxation time is

$$\tau = \frac{2}{k_B T} \sum_k \frac{E(k)}{\Gamma_1(k)+\Gamma_2(k)} f_{\rm eq}(k) \Big/ \sum_k f_{\rm eq}(k) , \quad (31)$$

where $E(k)$ is the parabolic electron energy band and $f_{\rm eq}(k)$ is the equilibrium electron distribution function. The scattering rates Γ_1 and Γ_2 are the approximate scattering-out rates given in Eq. (28) and (29). Electron drift velocities are low in comparison with bulk silicon. It is important that scattering by emission of excited quantum-confined phonons be retained in the treatment of quantum wires. If we consider scattering from only the lowest acoustic-phonon branch, we see that the scattering-out rate Γ_1 is proportional to A. Consequent-

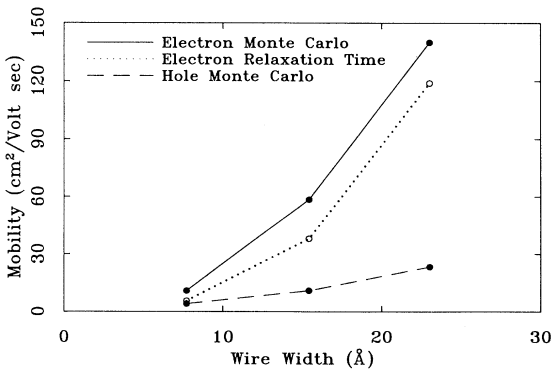

FIG. 7. Low-field electron and hole mobilities as functions of wire size at 300 K. The electron and hole mobilities are obtained from the Monte Carlo calculation by taking the slope of the velocity-field curves at low fields. A relaxation-time estimate for the electron mobility is shown for comparison.

ly, the relaxation time and mobility would be proportional to the area of the wire in the absence of other scattering mechanisms. Scattering involving excited quantum-confined phonons, however, is important even though these bands are not appreciably populated at room temperature. Electron scattering by emission of quantum-confined phonons greatly enhances the total scattering-out rate when $E(k)$ exceeds the excited phonon energy. The relaxation-time estimates for electron mobilities are indicated in Fig. 7, in fair agreement with the Monte Carlo results.

E. Drift velocities

For each of the wire sizes studied, we compute room-temperature electron and hole drift velocities as functions of the applied electric field. Velocity field curves for electrons at 300 K are shown in Fig. 8(a) for wire widths between 7.7 and 23 Å. For electric fields up to 50 kV/cm, only the four lowest-lying pseudodirect valleys are significantly populated. The drift velocities are seen to be Ohmic at low fields. At higher fields, a velocity saturation effect is seen in the 23-Å wire which we attribute to a combination of nonparabolicity effects and scattering of electrons into the low-lying indirect valley at $0.3\pi/a$.

Unfortunately, negative differential mobility is not seen in these curves. This is attributable to two effects: (1) the mobility goes down as the wire becomes smaller and (2) the satellite valley separation energy goes up as the wire size becomes smaller. Both of these effects combine to inhibit the transfer of electrons into the satellite valleys as the wire size becomes smaller. These results suggest that the optimum condition for observing negative differential mobility is for high mobilities (i.e., low temperatures) and small valley separation (i.e., large wires or bulk silicon). Indeed, bulk silicon at low temperature does exhibit a small negative differential mobility.[17]

In Fig. 8(b) the hole drift velocities are shown as a function of the applied electric field for wire widths between 7.7 and 23 Å. At room temperature and for fields up to 50 kV/cm, only the four highest-lying valence subbands contribute significantly to the total hole drift velocity. The valence subbands are highly nonparabolic, the hole distributions are spread out over a large region of k space, and the scattering-out rates are strongly k dependent. Consequently, it is difficult to interpret hole drift velocities in terms of effective masses and scattering rates for carriers residing in a parabolic valley.

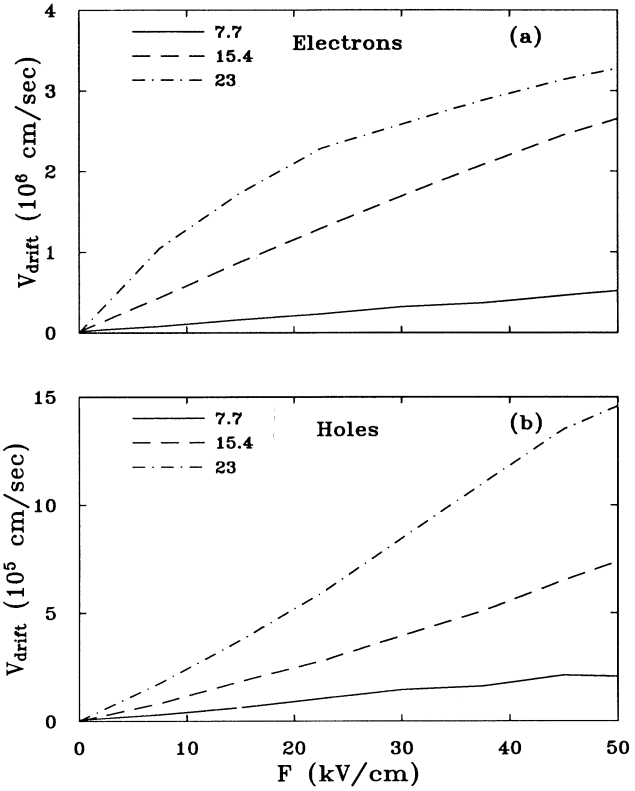

FIG. 8. Velocity-field curves at 300 K for 7.7-, 15.4-, and 23-Å silicon quantum wires. Electron velocity-field curves are shown in (a) and hole velocity-field curves are shown in (b).

IV. CONCLUSIONS

We calculate transport properties of idealized silicon wires using the Monte Carlo Method. The quantum wire subbands and wave functions are computed in a realistic tight-binding model, which yields subbands and tight-binding wave functions. Assuming deformation-potential acoustic-phonon scattering, we compute scattering rates between tight-binding initial and final states within the framework of Fermi's golden rule.

Although bulk silicon is indirect, the silicon wire band structure is pseudodirect with an X-like conduction-band minimum and Γ-like valence-band maximum at the zone center. The electron and hole subbands are highly nonparabolic with the lowest-lying electron masses much smaller than the lowest-lying hole masses. Electron mobilities are found to be approximately five time larger than hole mobilities and the computed low-field mobilities increase with wire size.

ACKNOWLEDGMENTS

We thank P. Kumar, A. V. Kuznetsov, D. B. Tanner, J. L. Musfeldt, and Jack Higman for useful comments. This work was supported by the National Science Foundation through Grant No. DMR8957382 and the U.S. Office of Naval Research through Grant No. N00091-J-1956. C.J.S. gratefully acknowledges the assistance of the Alfred P. Sloan Foundation.

[1]L. T. Canham, Appl. Phys. Lett. **57**, 1046 (1990).
[2]V. Lehmann and U. Gösele, Appl. Phys. Lett. **58**, 856 (1991).
[3]G. D. Sanders and Y. C. Chang, Phys. Rev. B **45**, 9202 (1992).
[4]G. D. Sanders and Y. C. Chang, Appl. Phys. Lett. **60**, 2525 (1992).
[5]M. S. Hybertsen, in *Light Emission from Silicon,* edited by S. S. Iyer, R. T. Collins, and L. T. Canham, MRS Symposia Proceedings No. 256 (Materials Research Society, Pittsburgh,

1992), p. 179.
[6]M. S. Hybertsen and M. Needles, Phys. Rev. B **48**, 4608 (1993).
[7]R. A. Smith, *Semiconductors,* 2nd ed. (Cambridge University Press, Cambridge, 1978), p. 394.
[8]D. Jovanovic and J. P. Leburton, in *Monte Carlo Device Simulation: Full Band and Beyond,* edited by K. Hess (Kluwer Academic, Boston, 1991), pp. 191–218.
[9]M. V. Fischetti and J. M. Higman, in *Monte Carlo Device Simulation: Full Band and Beyond* (Ref. 8), pp. 123–160.
[10]C. Jacoboni and L. Reggiani, Rev. Mod. Phys. **55**, 645 (1983).
[11]D. W. Bailey and C. J. Stanton, Phys. Rev. B **42**, 3423 (1990).
[12]*Monte Carlo Device Simulation: Full Band and Beyond* (Ref. 8).
[13]P. Vogel, H. P. Hjalmarson, and J. D. Dow, J. Phys. Chem. Solids **44**, 365 (1983).
[14]J. P. Walker and M. L. Cohen, Phys. Rev. **183**, 763 (1969).
[15]W. A. Harrison, *Electronic Structure and the Properties of Solids* (McGraw-Hill, New York, 1980).
[16]M. Lundstrom, *Fundamentals of Carrier Transport* (Addison-Wesley, New York, 1990).
[17]C. Canali *et al.*, in *Hot Electron Transport in Semiconductors,* edited by L. Reggiani (Springer-Verlag, Berlin, 1985), p. 99.